Journal of Power Sources 216 (2012) 22–27

Contents lists available at SciVerse ScienceDirect

Journal of Power Sources

journal homepage: www.elsevier.com/locate/jpowsour

Short communication

Microwave hydrothermal synthesis of high performance tin–graphene nanocomposites for lithium ion batteries

Shuangqiang Chen [a,b], Yong Wang [a,**], Hyojun Ahn [c], Guoxiu Wang [b,*]

[a] School of Environmental and Chemical Engineering, Shanghai University, Shangda Road 99, Shanghai 200444, PR China
[b] Centre for Clean Energy Technology, School of Chemistry and Forensic Science, University of Technology Sydney, Broadway, Sydney, NSW 2007, Australia
[c] School of Materials Science and Engineering, Gyeongsang National University, 900 Gazwa-dong, Jinju, Gyeongnam 660-701, Republic of Korea

HIGHLIGHTS

- Sn–GNS were prepared by a microwave hydrothermal synthesis and a one-step H_2 reduction.
- Sn nanoparticles are homogenously sandwiched between highly conductive and flexible GNS.
- Altering the ratio between tin and graphene had critical influences on their morphologies.
- Sn–GNS exhibited a high lithium storage capacity of 1407 mAh g^{-1}.

ARTICLE INFO

Article history:
Received 13 February 2012
Received in revised form
20 April 2012
Accepted 21 May 2012
Available online 28 May 2012

Keywords:
Graphene nanosheets
Tin nanoparticles
Microwave hydrothermal synthesis
Hydrogen reduction
Lithium ion batteries

ABSTRACT

Tin–graphene nanocomposites are prepared by a combination of microwave hydrothermal synthesis and a one-step hydrogen gas reduction. Altering the weight ratio between tin and graphene nanosheets has critical influences on their morphologies and electrochemical performances. Field emission scanning electron microscope (FESEM) and transmission electron microscope (TEM) analysis confirm the homogeneous distribution of tin nanoparticles on the surface of graphene nanosheets. When applied as an anode material in lithium ion batteries, tin–graphene nanocomposite exhibits a high lithium storage capacity of 1407 mAh g^{-1}. The as-prepared tin–graphene nanocomposite also demonstrates an excellent high rate capacity and a stable cycle performance. The superior electrochemical performance could be attributed to the synergistic effect of the three-dimensional nanoarchitecture, in which tin nanoparticles are sandwiched between highly conductive and flexible graphene nanosheets.

1. Instruction

Lithium-ion batteries are widely used as the power sources for portable electronic devices, owing to their high energy density, high voltage and long cycle life than other rechargeable batteries. The electrochemical performances of lithium ion batteries are determined by both cathode materials and anode materials. For large-scale applications such as electric vehicles, new electrode materials must be developed to meet the increasing demand for high energy density and power density.

Carbon-based materials are the commercial anode materials for Li-ion batteries [1] with a limited theoretical capacity of 372 mAh g^{-1}, which cannot meet the demand for high specific capacities. Metal and metal oxides, such as silicon (Si) [2], tin (Sn) [3,4], cobalt oxide (Co_3O_4) [5–8], and nickel oxide (NiO) [6,8–10], have been considered as promising alternative anode materials for reversible lithium storage. In particular, metallic tin and tin based anode materials [11–15] are one of the attractive replacement materials for lithium ion batteries due to their high theoretical capacity ≥992 mAh g^{-1}. On the other hand, tin and tin based anode materials do not encounter solvent intercalation during discharge/charge cycling, leading to greatly reduced irreversible capacity loss, while large volume variation always occurs in tin based anode materials during lithiation and de-lithiation processes, which causes pulverization of the electrode [16–18]. In order to overcome this problem, many methods have been developed to buffer or prevent volume changes such as CNTs-encapsulation [17,19], formation of core–shell nanostructures [2,20–23], and decrease of particle size [24].

Graphene, discovered by Geim and Novoselov [25] in 2004, is an allotrope of carbon with a structure of one-atom-thick planar sheet

* Corresponding author. Tel: +61 2 95141741; fax: +61 2 95141460.
** Corresponding author.
E-mail addresses: yongwang@shu.edu.cn (Y. Wang), Guoxiu.wang@uts.edu.au (G. Wang).

0378-7753/$ – see front matter © 2012 Elsevier B.V. All rights reserved.
doi:10.1016/j.jpowsour.2012.05.051

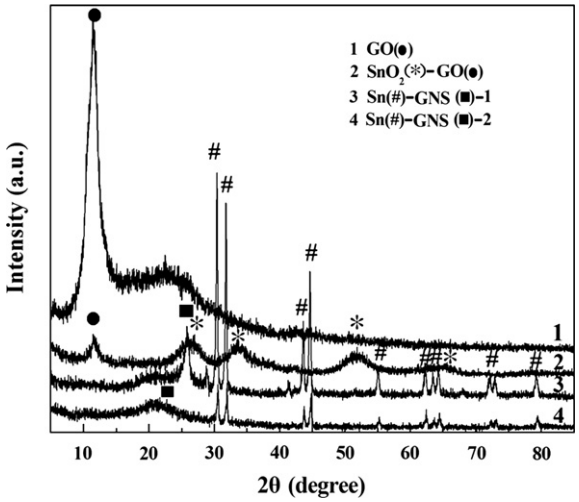

Fig. 1. Powder X-ray diffraction (XRD) patterns of graphite oxide (GO), SnO_2–graphene oxide (SnO_2–GO), Sn–GNS-1 and Sn–GNS-2.

of sp^2-bonded carbon. Many studies have demonstrated that graphene possesses outstanding physical, chemical and mechanical properties [26–30]. It has been proved that lithium ions could be absorbed on the two sides of graphene nanosheet, which increases the theoretical capacity to 744 mAh g^{-1} [31–35] according to the formation of Li_2C_6. Graphene nanosheet (GNS)-based materials have been investigated for lithium storage. Ji and co-worker [36] prepared a multilayer nanoassembly of Sn-nanopillar with graphene, which formed three-dimensional (3D) structure without polymer binder and carbon black. The initial reversible specific capacity reached 734 mAh g^{-1}. The specific capacity maintained 679 mAh g^{-1} after 30 cycles. Li and coworkers [37] reported that graphite oxide (GO) was simply reduced by Sn^{2+} ion, forming SnO_2/graphene anode materials with different weight ratios. It was found that different ratios between Sn^{2+} and GO led to different morphologies and specific capacities. In particular, the specific capacity reached 541.3 mAh g^{-1} at a current density of 200 mA g^{-1} in a voltage range of 1.5–0.01 V. Kim and co-workers [38] developed a SnO_2/graphene composite via loading Sn particles on GO, then reduced by NH_4OH and hydrazine at 80 °C for 8 h. The first reversible specific capacity was about 852 mAh g^{-1} and retained 634 mAh g^{-1} after 50 cycles at a current density of 100 mA g^{-1} between 0.001 and 3.0 V. When the current density was increased to 2000 mA g^{-1}, the reversible specific capacity was 389 mAh g^{-1}.

Microwave-assisted hydrothermal synthesis (MAHS) method has many advantages such as fast heating, high yield rate, and good homogeneity. Both cathode and anode materials for lithium ion batteries with novel structures and special morphologies have been prepared by the MAHS method and demonstrated improved properties [39–41]. Most of the previous reports involved in the preparation of SnO_2–graphene nanocomposites. Zhong et al. synthesized SnO_2–graphene composites and achieved a stable capacity of 590 mA g^{-1} at a current density of 100 mAh g^{-1} [41]. Zhu and coworkers developed SnO_2–graphene composites, in which tin oxide particles (100–200 nm) uniformly anchored on the surface of graphene [42]. Herein, we report a simple and novel synthetic route to prepare Sn–graphene nanocomposites using a combination of microwave hydrothermal reaction and H_2 reduction. The homogeneous dispersion of Sn nanoparticles on graphene nanosheets was achieved by the MAHS method. The as-prepared Sn–graphene nanocomposites exhibited a better electrochemical performance for lithium storage in lithium ion batteries than that of the previously reported results.

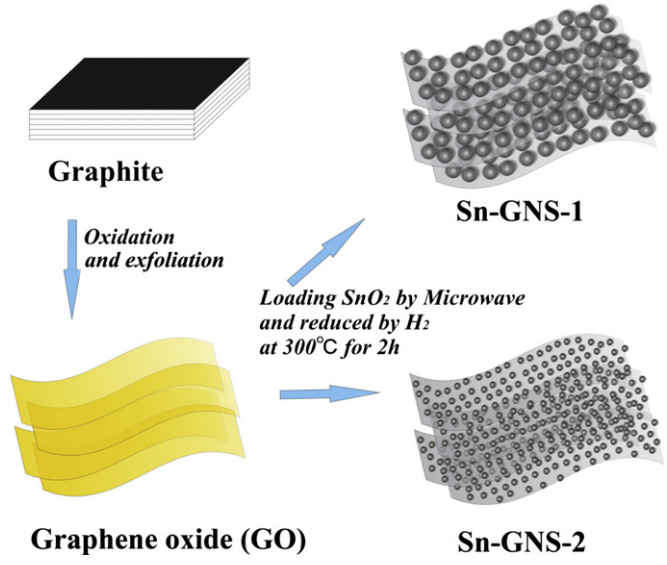

Fig. 2. A schematic illustration for the preparation process of Sn–graphene (Sn–GNS) nanocomposites.

2. Experimental

Graphene oxide (GO) was prepared according to the previously published procedure [43]. Two batches of Sn–graphene nanosheets (Sn–GNS) composites were synthesized with weight ratios of 1:1

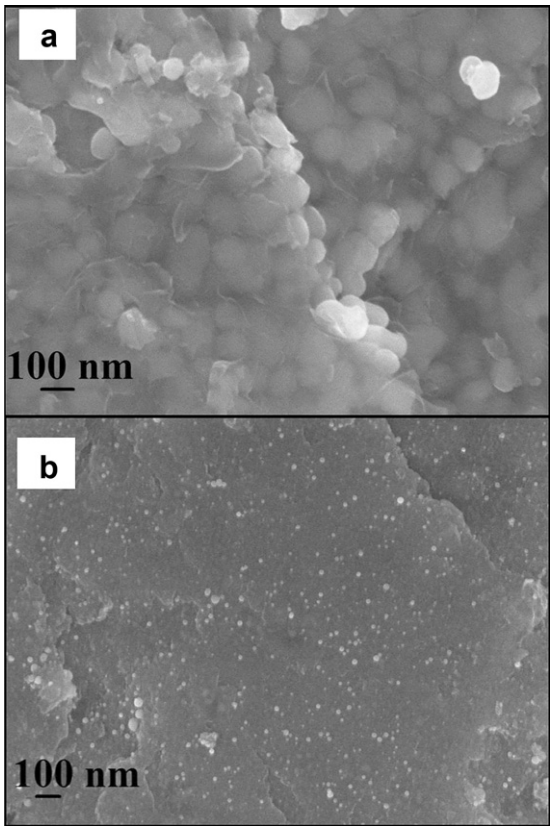

Fig. 3. SEM images of Sn–graphene nanocomposites: (a) Sn–GNS-1, (b) Sn–GNS-2.

and 1:4, which are defined as Sn–GNS-1 and Sn–GNS-2, respectively. For the preparation of Sn–GNS composites, 20 ml 0.0072 M $SnCl_4 \cdot 5H_2O$ aqueous solution was added into the two certain amount of GO (14 ml and 56 ml, 2 mg ml^{-1}) solutions. After mixing by ultrasonic probe for 1 h, the solutions were transferred to another beaker. Excessive amount of urea was added into the solutions. Then, the solutions were heated in the single mode of microwave reactor (NOVA I microwave synthesizer with a magneton stirring and monitoring the real pressure in the vessel) at 120 °C for 20 min. The precursors of SnO_2–GO were obtained. The precipitates were collected by centrifugation and washed with de-ionized water for several times. The dried precursors (SnO_2–GO-1 and SnO_2–GO-2) and GO were heated at 300 °C for 2 h in a quartz tube furnace under a flowing gas mixture of H_2 in N_2 (H_2: 10%, N_2: 90%) at a flow rate of 80 sccm, respectively. The actual ratios of tin:graphene have been determined by the CHN elemental analysis. The Sn–GNS-1 consists of 51.4 wt.% carbon, which is close to the weight ratio Sn:C = 1:1. The Sn–GNS-2 sample consists of 80.7 wt.% carbon, corresponding to the weight ratio Sn:C = 1:4.

Sn–graphene nanocomposites and GNS were characterized by X-ray diffraction (XRD, Rigaku D/max-2550V, Cu Kα radiation), field-emission scanning electron microscopy (FESEM, JSM-6700F), and transmission electron microscopy/selected area electron diffraction (TEM/SAED, JEOL JEM-200CX and JEM-2010F).

For electrochemical testing, the working electrodes were made by mixing 80 wt.% active material, 10 wt.% acetylene black, and 10 wt.% binder (polyvinylidene difluoride) in NMP to form a slurry. Then, the slurry was coated on copper foil and dried in a vacuum oven at 65 °C for 12 h. Swagelok cells with a diameter of 12 mm were assembled in an argon-filled glove-box (Mbraun, Unilab, Germany), in which both the moisture and oxygen contents were controlled to be less than 0.1 ppm. Lithium foil was used as the counter electrode and the electrolyte was 1 M $LiPF_6$ in a 1:1 (weight ratio) mixture of ethylene carbonate and diethyl carbonate. Electrochemical measurements were performed on a LAND-CT2001C battery test system. The cells were galvanostatically discharged and charged in the fixed voltage range of 0.005–3.0 V, with a current density of 100 mAh g^{-1} (0.1 C). Higher current densities (0.5 C, 1 C, 2 C and 5 C) were also used to test the high rate capability.

3. Results and discussion

The properties of the graphene oxide (GO), SnO_2–graphene oxide (SnO_2–GO), Sn–GNS-1, and Sn–GNS-2 were characterized by X-ray diffraction (XRD) and the XRD patterns were showed in Fig. 1. The characteristic peak of graphene oxide at 11.5° corresponds to the (002) planes of graphite oxide, indicating that the

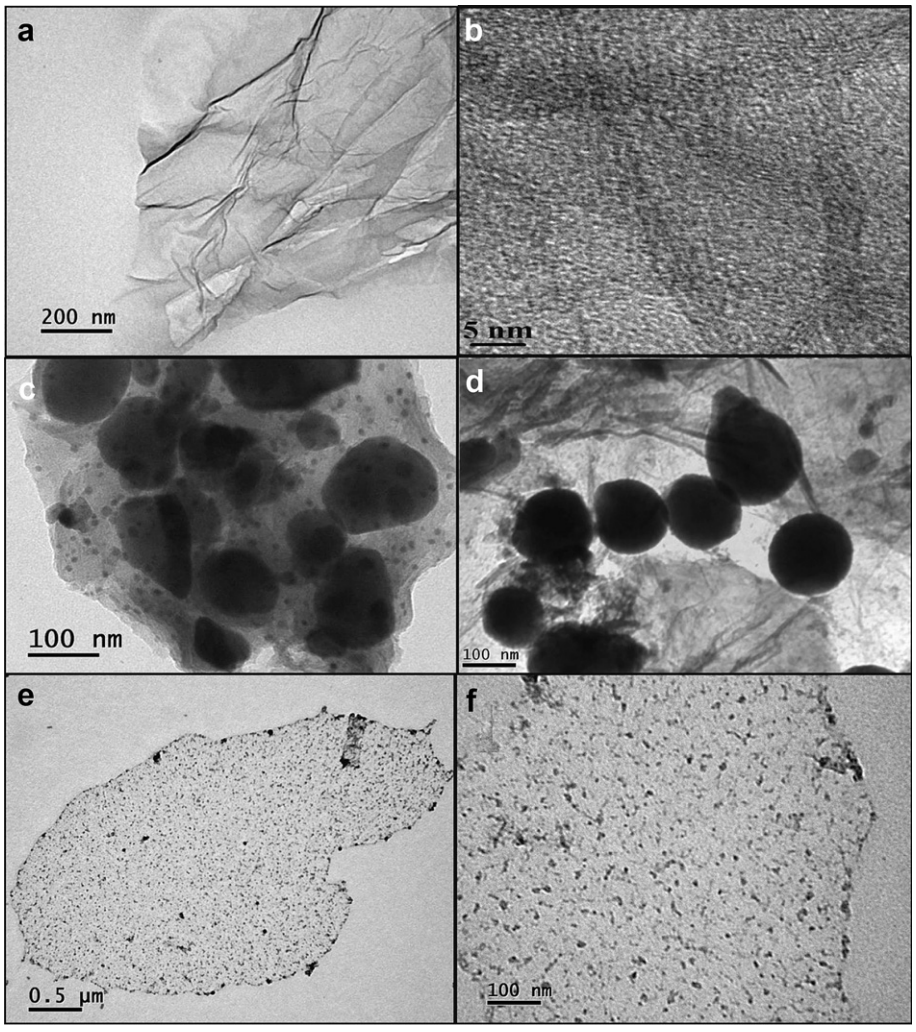

Fig. 4. (a) TEM image of graphene nanosheets (GNS), (b) HRTEM image of graphene nanosheets (GNS), (c,d) TEM images of Sn–GNS-1, (e,f) TEM images of Sn–GNS-2.

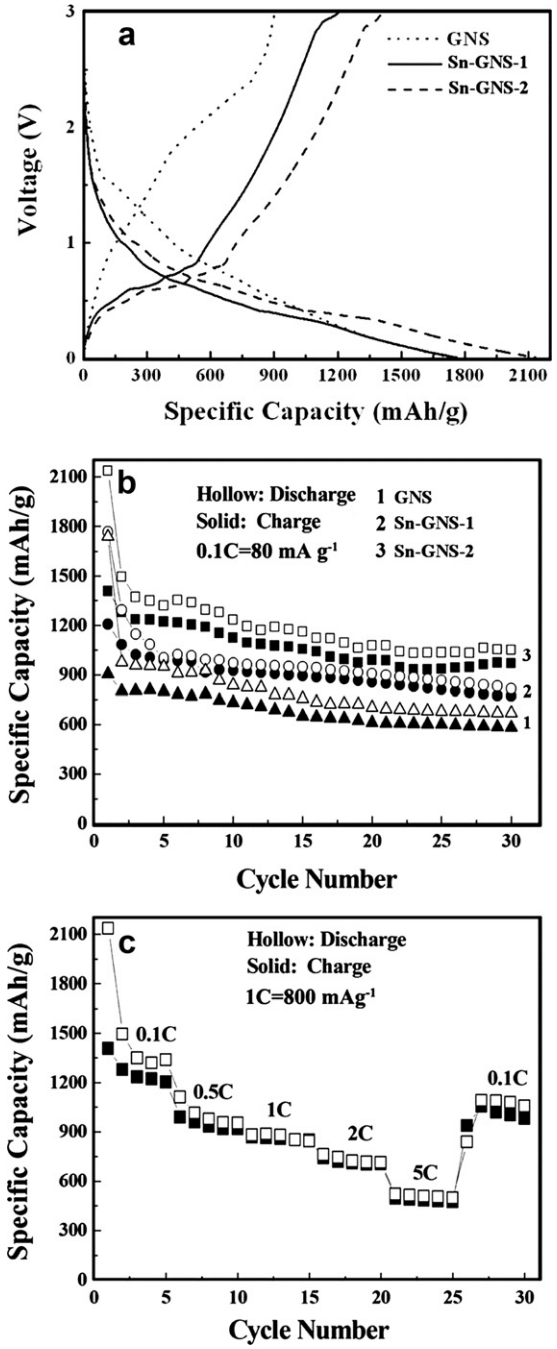

Fig. 5. Electrochemical performances of graphene nanosheets and Sn–graphene nanocomposites. (a) The discharge (lithium insertion) and charge (lithium extraction) curves of GNS, Sn–GNS-1 and Sn–GNS-2. (b) Cycling performances of GNS, Sn–GNS-1 and Sn–GNS-2 at 0.1 C. (c) Cycling performance of Sn–GNS-2 at stepwise current densities.

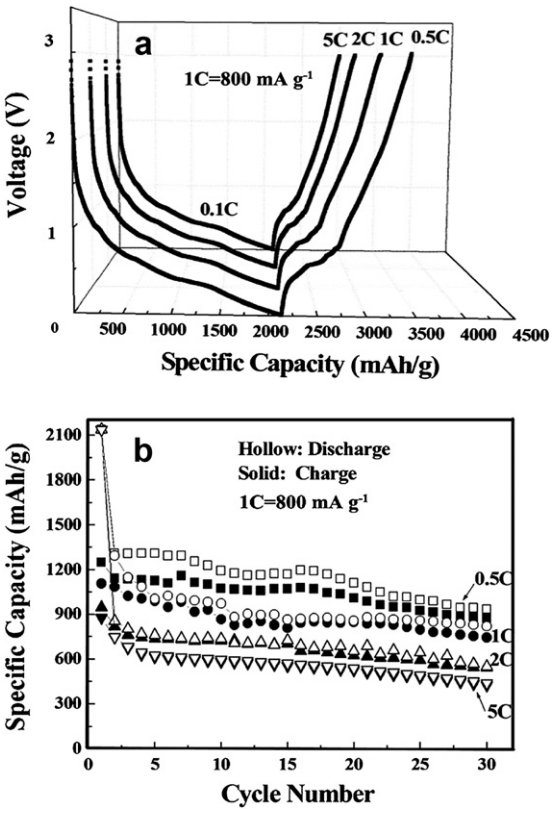

Fig. 6. (a) The discharge and charge curves of Sn–GNS-2 electrodes in the first cycle at current densities of 0.5 C, 1 C, 2 C and 5 C. (b) Cycling performances of Sn–GNS-2 electrodes at different current rates.

interplanar spacing of d_{002} had been expanded to 0.769 nm after oxidation. This is ascribed to the oxygen-containing functional groups that were attached, which has been previously confirmed by FTIR [32]. After heating by a single mode of microwave, the precursors were converted to SnO_2–GO, the characteristic peaks of GO were reserved and the other diffraction peaks can be indexed to the tetragonal rutile SnO_2 phase with lattice parameters $a = 4.738$ Å and $c = 3.188$ Å (JCPDS 21-1250). The broad diffraction peaks of SnO_2 indicate that the SnO_2 particles have small crystal size. The third and the firth XRD patterns are Sn–GNS nanocomposites with weight ratios of 1:1 and 1:4, respectively. The sharp diffraction lines reflect good crystallite of Sn obtained by H_2 reduction, moreover, he characteristic (002) diffraction peak of GO has shifted from 11.4° to 26.3°, confirming the reduction of graphene oxide to graphene nanosheets.

A schematic representation of the synthesis process was given, which can be observed in Fig. 2. The natural graphite powders were oxidized and exfoliated to graphene oxide by using the modified Hummers method [44]. When $SnCl_4$ and urea were added into graphene oxide solution, Sn^{4+} ions attached to the both sides of the basal plane of graphene oxide nanosheets, owing to the negatively charging nature of graphene oxide. Under microwave irradiation at 120 °C, $Sn(OH)_4$–GO precursors were formed initially and then converted to SnO_2–GO due to the effect of microwave energy. During the heat treatment in H_2 atmosphere, GO and SnO_2 nanoparticles were simultaneously reduced by H_2 at 300 °C to GNS and Sn nanoparticles. Therefore, the one-step H_2 reduction [45–47] can produce Sn–GNS nanocomposites with a uniform distribution of Sn nanoparticles on GNS.

The morphologies of Sn–GNS nanocomposites were observed by FESEM (as shown in Fig. 3). When the ratio of Sn and GNS was reduced to 1:4, smaller Sn nanoparticles with a uniform size of 10–20 nm were obtained (as shown in Fig. 3b). Since the melting point of Sn nanoparticles is 231.9 °C, SnO_2 nanoparticles were reduced to Sn nanoparticles by H_2 at 300 °C. Sn droplets adopt the sphere-like shape under the influence of the surface tension. Meanwhile, GO and SnO_2 nanoparticles were reduced simultaneously, which would be advantageous in maintaining the stability of the Sn–GNS nanocomposites.

In order to characterize the microstructure of GNS, transmission electron microscope (TEM) and high resolution transmission

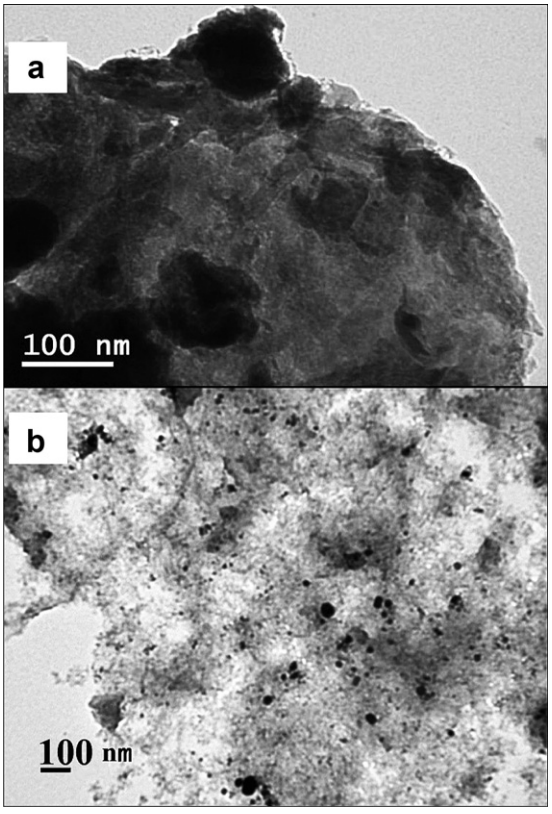

Fig. 7. (a) TEM image of Sn–GNS-1 after cycling test. (b) TEM image of Sn–GNS-2 after cycling test.

electron microscope (HRTEM) were used and the images of GNS were showed in Fig. 4(a) and (b), respectively. Under the electron beam, GNS exhibit a transparent feature with a winkle structure and a thickness of 3–5 nm, which corresponds to ~8–15 layers of single graphene nanosheets stacking together. The high magnification TEM images of Sn–GNS-1 (with a weight ratio of 1:1) nanocomposite were exhibited in Fig. 4(c) and (d). The Sn particles, with the diameters of 60–120 nm, scattered on the surfaces of graphene nanosheets. A large amount of Sn nanoparticles, with diameters of 10–20 nm, were also observed on the surfaces of GNS. Under the heat treatment at 300 °C, Sn nanoparticles become spherical with some aggregations. Furthermore, the aggregation phenomenon may also result from the high ratio of Sn–GNS (1:1), however, when the weight ratio of Sn and GNS was reduced to 1:4, the Sn nanoparticles obtained are much smaller and uniformly distributed on graphene nanosheets (as shown in Fig. 4(e) and (f)).

The electrochemical performances of GNS and Sn–GNS nanocomposites were tested by galvanostatical charge and discharge cycling in the voltage range of 0.005–3 V (at a current density of 80 mA g^{-1}). Fig. 5(a) shows the voltage profiles of GNS, Sn–GNS-1 and Sn–GNS-2 electrodes in the first cycle. The initial discharge and charge capacities of the GNS electrode are 1787 mAh g^{-1} and 904 mAh g^{-1}, corresponding to a Coulombic efficiency of 50.6%. The high lithium storage capacity could be attributed to a large amount of active sites such as edge-type sites, nano-cavities, or other defects in graphene nanosheets. There is a considerable capacity loss in forming solid electrolyte interphase (SEI) layers on the surface of GNS. The Sn–GNS-1 and Sn–GNS-2 electrodes delivered discharge capacities of 1776 and 2136 mAh g^{-1} and the charge capacities of 1206 and 1407 mAh g^{-1} with the Coulombic efficiencies of 67.9% and 65.9%, respectively. The high specific capacities of Sn–GNS composites could be ascribed to the contributions of Sn nanoparticles and the 3D stacking structure. There are a large amount of defects or nanocavities in GNS induced during the oxidation and reduction processes. It has been proposed that Li^+ ions could be adsorbed either on the surface or on the edge planes of the GNS [48]. In the first cycle, the irreversible capacities loss for Sn–GNS-1 and Sn–GNS-2 electrodes could be caused by the formation of the SEI layers on the surface of the electrodes, the large volume expansion of Sn nanoparticles, different content of Sn nanoparticles, and different surface areas of Sn–GNS nanocomposites. Moreover, the small plateaus at the end of the discharge process for Sn–GNS-1 and Sn–GNS-2 electrodes should be ascribed to the reaction of lithium with Sn nanoparticles. This phenomenon has been reported in the previous publications [23,49]. The cycle performances of the GNS, Sn–GNS-1 and Sn–GNS-2 samples are shown in Fig. 5(b). After 30 cycles, the specific capacities of GNS, Sn–GNS-1 and Sn–GNS-2 electrodes are 582 mAh g^{-1}, 771.8 mAh g^{-1} and 1100 mAh g^{-1}, respectively. These corresponds to the capacity retention ratios of 64.3%, 63.9% and 78.1%. Therefore, Sn–GNS-2 electrode demonstrated the best cycle performance. The better cycling performance of the sample Sn–GNS-2 could be attributed to small Sn nanoparticles and the synergistic effect of the Sn–GNS 3D nanoarchitecture. The volume change of Sn nanoparticles can be effectively buffered by flexible graphene nanosheets, which maintains the integrity of the electrode on charge and discharge cycling. In order to examine the tolerance of the Sn–GNS nanocomposite electrode towards different current densities, the Sn–GNS-2 electrode was cycled at different current densities (0.1 C, 0.5 C, 1 C, 2 C, and 5 C) and reversed back to low current densities (Fig. 5(c)). As expected, the capacity decreases with increasing current densities. It should be noted that when the current density was reversed back to a low current density, the capacity almost recover to the original value. This indicates that the Sn–GNS nanocomposites are quite tolerant to the high current charge and discharge.

The voltage profiles of Sn–GNS-2 nanocomposite electrode at different current densities in the first cycle can be seen in the Fig. 6(a). The electrode delivered specific discharge capacities of 1247, 1106, 946 and 876 mAh g^{-1} at current densities of 0.5 C, 1 C, 2C and 5 C, respectively. After 30 cycles, the Sn–GNS-2 electrode maintained a specific capacity of 542 mAh g^{-1} at the current density of 1600 mA g^{-1} and a reversible capacity of 423 mAh g^{-1} at the current density of 4000 mA g^{-1}. The shapes of voltage profiles are similar for four pairs of discharge and charge curves. In order to further illustrate the cycle performances of Sn–GNS-2 nanocomposite electrode at different current densities, the electrochemical cycle performances are tested and showed in Fig. 6(b). The Sn–GNS nanocomposites electrodes have demonstrated a good rate performance under high current charge and discharge cycling.

After 30 cycles, the Sn–GNS electrodes were examined by TEM analysis. The TEM images of two Sn–GNS nanocomposite electrode after cycling can clearly illustrate the properties of the two electrodes. From Fig. 7(a), the pulverization and cracking of Sn nanoparticles can be easily identified. This could be due to relatively large particle size of Sn (60–120 nm) in the Sn–GNS-1 sample, which cannot endure large volume change on cycling. On the contrary, there is no apparent crack on Sn nanoparticles in the sample Sn–GNS-2 electrode after cycling test (as shown in Fig. 7(b)), which could be credited to the much smaller size of Sn nanoparticles (5–15 nm). Therefore, it is essential to obtain small Sn nanoparticles and uniform distribution on GNS to achieve good electrochemical performance.

4. Conclusions

We have developed a microwave hydrothermal synthesis approach for the preparation of Sn–GNS nanocomposites with different weight ratio using hydrogen gas reduction. Altering the

weight ratio between tin and graphene has critical influences on their morphologies. Field emission scanning electron microscope (FESEM) and transmission electron microscope (TEM) analysis reveals that tin nanoparticles homogeneously distribute on the surface of graphene nanosheets. There is no apparent pulverization and cracking of Sn nanoparticles for Sn–graphene nanosheets nanocomposite after cycling test. The Sn–graphene nanosheets with weight ratio of 1:4 (Sn–GNS-2) exhibits a high initial reversible specific capacity of 946 mAh g^{-1} at large current density of 1600 mA g^{-1} and a high specific capacity of 542 mAh g^{-1} has been maintained after 30 cycles, which demonstrates that the Sn–GNS-2 electrode has an excellent high rate capacity and a stable cycle performance. The superior electrochemical performance should be attributed to the high specific surface area of tin nanoparticles and the synergetic effect of the combination of Sn nanoparticles and highly conductive graphene nanosheets.

Acknowledgement

The authors gratefully acknowledge the financial support from Australian Research Council (ARC) through the ARC Discovery project (DP1093855), the National Natural Science Foundation of China (50971085, 50701029), the Professor of Special Appointment (Eastern Scholar), the Chinese Scholarship Council, and the National Research Foundation of Korea through the WCU (World Class University) Program (R32-2008-000-20093-0).

References

[1] R. Malini, U. Uma, T. Sheela, M. Ganesan, N.G. Renganathan, Ionics 15 (2009) 301.
[2] L.F. Cui, R. Ruffo, C.K. Chan, H.L. Peng, Y. Cui, Nano Lett. 9 (2009) 491.
[3] I.T. Lucas, E. Pollak, R. Kostecki, Electrochem. Commun. 11 (2009) 2157.
[4] Y. Wang, J.Y. Lee, B.H. Chen, J. Electrochem. Soc. 151 (2004) A563.
[5] F.D. Wu, M.H. Wu, Y. Wang, Electrochem. Commun. 13 (2011) 433.
[6] H. Cheng, Z.G. Lu, J.Q. Deng, C.Y. Chung, K. Zhang, Y.Y. Li, Nano Res. 3 (2010) 895.
[7] F.F. Tao, C.L. Gao, Z.H. Wen, Q. Wang, J.H. Li, Z. Xu, J. Solid State Chem. 182 (2009) 1055.
[8] D.Y. Kim, H.J. Ahn, J.S. Kim, I.P. Kim, J.H. Kweon, T.H. Nam, K.W. Kim, J.H. Ahn, S.H. Hong, Electron. Mater. Lett. 5 (2009) 183.
[9] J.S. Do, R.F. Dai, J. Power Sources 189 (2009) 204.
[10] X.H. Huang, J.P. Tu, X.H. Xia, X.L. Wang, J.Y. Xiang, L. Zhang, Y. Zhou, J. Power Sources 188 (2009) 588.
[11] Y. Wang, J.Y. Lee, T.C. Deivaraj, J. Electrochem. Soc. 151 (2004) A1804.
[12] Y. Wang, J.Y. Lee, J. Power Sources 144 (2005) 220.
[13] Y. Wang, J.Y. Lee, Electrochem. Commun. 5 (2003) 292.
[14] S.J. Han, B.C. Jang, T. Kim, S.M. Oh, T. Hyeon, Adv. Funct. Mater. 15 (2005) 1845.
[15] S.-M. Paek, E. Yoo, I. Honma, Nano Lett. 9 (2009) 72.
[16] J. Hassoun, G. Derrien, S. Panero, B. Scrosati, Adv. Mater. 20 (2008) 3169.
[17] G. Derrien, J. Hassoun, S. Panero, B. Scrosati, Adv. Mater. 19 (2007) 2336.
[18] H.-X. Zhang, C. Feng, Y.-C. Zhai, K.-L. Jiang, Q.-Q. Li, S.-S. Fan, Adv. Mater. 21 (2009) 2299.
[19] F.D. Wu, Y. Wang, J. Mater. Chem. 21 (2011) 6636.
[20] F. Wu, J.Z. Chen, R.J. Chen, S.X. Wu, L. Li, S. Chen, T. Zhao, J. Phys. Chem. C 115 (2011) 6057.
[21] A. Basch, J.H. Albering, J. Power Sources 196 (2011) 3290.
[22] Z.X. Chen, Y.L. Cao, J.F. Qian, X.P. Ai, H.X. Yang, J. Mater. Chem. 20 (2010) 7266.
[23] S. Chen, P. Chen, M. Wu, D. Pan, Y. Wang, Electrochem. Commun. 12 (2010) 1302.
[24] Z.L. Yang, C. Cao, F.F. Liu, D.R. Chen, X.L. Jiao, Solid State Ionics 181 (2010) 678.
[25] A.K. Geim, K.S. Novoselov, Nat. Mater. 6 (2007) 183.
[26] A. Pirkle, J. Chan, A. Venugopal, D. Hinojos, C.W. Magnuson, S. McDonnell, L. Colombo, E.M. Vogel, R.S. Ruoff, R.M. Wallace, Appl. Phys. Lett. 99 (2011) 122108.
[27] J. Alicea, M.P.A. Fisher, Phys. Rev. B 74 (2006) 075422.
[28] D.C. Elias, R.R. Nair, T.M.G. Mohiuddin, S.V. Morozov, P. Blake, M.P. Halsall, A.C. Ferrari, D.W. Boukhvalov, M.I. Katsnelson, A.K. Geim, K.S. Novoselov, Science 323 (2009) 610.
[29] G. Wang, Y. Kim, M. Choe, T.W. Kim, T. Lee, Adv. Mater. 23 (2011) 755.
[30] B. Sun, B. Wang, D.W. Su, L.D. Xiao, H. Ahn, G.X. Wang, Carbon 50 (2012) 727.
[31] D.A. Abanin, S.V. Morozov, L.A. Ponomarenko, R.V. Gorbachev, A.S. Mayorov, M.I. Katsnelson, K. Watanabe, T. Taniguchi, K.S. Novoselov, L.S. Levitov, A.K. Geim, Science 332 (2011) 328.
[32] Y. Zhang, Y.-W. Tan, H.L. Stormer, P. Kim, Nature 438 (2005) 201.
[33] K. Xu, P. Cao, J.R. Heath, Science 329 (2010) 1188.
[34] M. Zhang, D. Lei, X. Yin, L. Chen, Q. Li, Y. Wang, T. Wang, J. Mater. Chem. 20 (2010) 5538.
[35] G.X. Wang, B. Wang, X.L. Wang, J. Park, S.X. Dou, H. Ahn, K. Kim, J. Mater. Chem. 19 (2009) 8378.
[36] L.W. Ji, Z.K. Tan, T. Kuykendall, E.J. An, Y.B. Fu, V. Battaglia, Y.G. Zhang, Eng. Environ. Sci. 4 (2011) 3611.
[37] Y.M. Li, X.J. Lv, J. Lu, J.H. Li, J. Phys. Chem. C 114 (2010) 21770.
[38] H. Kim, S.W. Kim, Y.U. Park, H. Gwon, D.H. Seo, Y. Kim, K. Kang, Nano Res. 3 (2010) 813.
[39] K.L. Harrison, A. Manthiram, Inorg. Chem. 50 (2011) 3613.
[40] S. Yoon, A. Manthiram, J. Mater. Chem. 21 (2011) 4082.
[41] C. Zhong, J.Z. Wang, Z.X. Chen, H.K. Liu, J. Phys. Chem. C 115 (2011) 25115.
[42] X. Zhu, Y. Zhu, S. Murali, M.D. Stoller, R.S. Ruoff, J. Power Sources 196 (2011) 6473.
[43] S.Q. Chen, Y. Wang, J. Mater. Chem. 20 (2010) 9735.
[44] W.S. Hummers, R.E. Offeman, J. Am. Chem. Soc. 80 (1958) 1339.
[45] X.Y. Wang, X.F. Zhou, K. Yao, J.G. Zhang, Z.P. Liu, Carbon 49 (2011) 133.
[46] S.Z. Liang, X.F. Zhu, P.C. Lian, W.S. Yang, H.H. Wang, J. Solid State Chem. 184 (2011) 1400.
[47] M. Zhang, D. Lei, Z.F. Du, X.M. Yin, L.B. Chen, Q.H. Li, Y.G. Wang, T.H. Wang, J. Mater. Chem. 21 (2011) 1673.
[48] A.V. Murugan, T. Muraliganth, A. Manthiram, Chem. Mater. 21 (2009) 5004.
[49] B.K. Guo, J. Shu, K. Tang, Y. Bai, Z.X. Wang, L.Q. Chen, J. Power Sources 177 (2008) 205.